

JGR Solid Earth

RESEARCH ARTICLE

10.1029/2020JB019696

Key Points:

- Variably serpentinized peridotites from the Zedang ophiolite in southern Tibet were magnetically and mineralogically examined
- We observed that magnetite formation is limited above ~50% serpentinization in the Zedang ophiolite
- The serpentinization may start at >250-300°C at an oceanic spreading ridge center and continue at <200-250°C in near-seafloor settings

Supporting Information:

- Supporting Information S1
- · Table S1

Correspondence to:

Z. Li and J. Zheng, zhiyonli@cug.edu.cn; jpzheng@cug.edu.cn

Citation:

Li, Z., Moskowitz, B. M., Zheng, J., Xiong, Q., Zhou, X., Yang, J., et al. (2020). Petromagnetic characteristics of serpentinization and magnetite formation at the Zedang ophiolite in southern Tibet. Journal of Geophysical Research: Solid Earth, 125, e2020JB019696. https://doi.org/ 10.1029/2020JB019696

Received 2 MAR 2020 Accepted 4 AUG 2020 Accepted article online 6 AUG 2020

Petromagnetic Characteristics of Serpentinization and Magnetite Formation at the Zedang Ophiolite in Southern Tibet

Zhiyong Li¹, Bruce M. Moskowitz², Jianping Zheng³, Qing Xiong³, Xiang Zhou³, Jingsui Yang⁴, Yuwen Zhang⁵, and Qingsheng Liu¹

¹Hubei Subsurface Multi-scale Imaging Key Laboratory, Institute of Geophysics and Geomatics, China University of Geosciences, Wuhan, China, ²Department of Earth and Environmental Sciences and Institute for Rock Magnetism, University of Minnesota, Twin Cities, Minneapolis, MN, USA, ³State Key Laboratory of Geological Processes and Mineral Resources, School of Earth Sciences, China University of Geosciences, Wuhan, China, ⁴Institute of Geology, Chinese Academy of Geological Sciences, Beijing, China, ⁵School of Geophysics and Information Technology, China University of Geosciences, Beijing, China

Abstract Variably serpentinized peridotites from the Zedang ophiolite in southern Tibet were magnetically and petrologically examined to understand the serpentinization process and evaluate the origin of magnetic anomalies in ultramafic-hosted tectonic settings. Magnetite occurs in the serpentine and brucite veins and is identified as the dominant magnetic carrier by thermomagnetic and petrological analyses. The magnetic susceptibility increases rapidly from <0.001 to ~0.02 SI for the <50% serpentinized samples followed by nearly constant values of 0.02–0.03 SI above 50% serpentinization. This transition corresponds with the formation of Fe-poor serpentine mesh (2–3 wt% FeO) and magnetite in the early stages and the replacement of mesh center olivine by Fe-rich serpentine (4–5 wt% FeO) without magnetite in the late stages. Brucite veins occur in the 50–70% serpentinized samples and indicate serpentinization temperatures from ~250 to <100°C. The serpentinization may initiate at an oceanic spreading ridge center under high temperatures (>250–300°C) to produce magnetite and subsequently continue at lower temperatures (<200–250°C) in near-seafloor settings and limit the magnetite formation, possibly associated with ophiolite emplacement. These serpentinized peridotites have higher magnetization intensities (average 2.26 Am⁻¹) than dolerite dykes and basaltic volcanics (mostly <1 A m⁻¹) in the area and should be the major source of aeromagnetic highs in the south Tibetan ophiolite belt.

1. Introduction

The magnetic signature of mantle serpentinization has crucial importance in interpreting the origin of high-amplitude magnetization anomalies at ultramafic-hosted hydrothermal settings (e.g., Blakely et al., 2005; Fujii et al., 2016; Szitkar & Murton, 2018). However, different groups of serpentinized peridotites from either oceanic lithosphere or ophiolite complexes on land often show large variations in the abundance of magnetite (e.g., Bonnemains et al., 2016; Oufi et al., 2002). The factors that control the formation of magnetite are many and include the degree of serpentinization (Bach et al., 2006; Oufi et al., 2002; Toft et al., 1990), iron partitioning and valance state in serpentine-brucite minerals (Evans et al., 2009; Klein et al., 2014), and physiochemical conditions during serpentinization such as fluid/rock ratio, silica activity, and temperature (Frost & Beard, 2007; Klein et al., 2009, 2014; McCollom et al., 2016).

The Yarlung-Zangbo ophiolite belt in southern Tibet extends over 2000 km from west to east (Figure 1a) and marks the closure of the Neo-Tethys Ocean between India and Asia during Mesozoic-Cenozoic times (e.g., Aitchison et al., 2000; Hébert et al., 2012). Large-scale positive aeromagnetic anomalies have been detected along this giant belt during geophysical surveys (Jiang et al., 2016; Wang et al., 2020; Yao et al., 2001), but magnetic studies of serpentinized ultramafic rocks are limited to few of the ophiolite bodies (He et al., 2014; Li et al., 2017). Here we present new data from rock magnetism, mineral chemistry, and petrographic microstructures of a suite of peridotite samples (from fresh to nearly complete serpentinization) collected from the Zedang ophiolite in the eastern part of the Yarlung-Zangbo ophiolite belt. The conditions of serpentinization and magnetite formation together with the magnetic sources at ophiolite complexes are synthesized and discussed.

©2020. American Geophysical Union. All Rights Reserved.

LI ET AL. 1 of 15

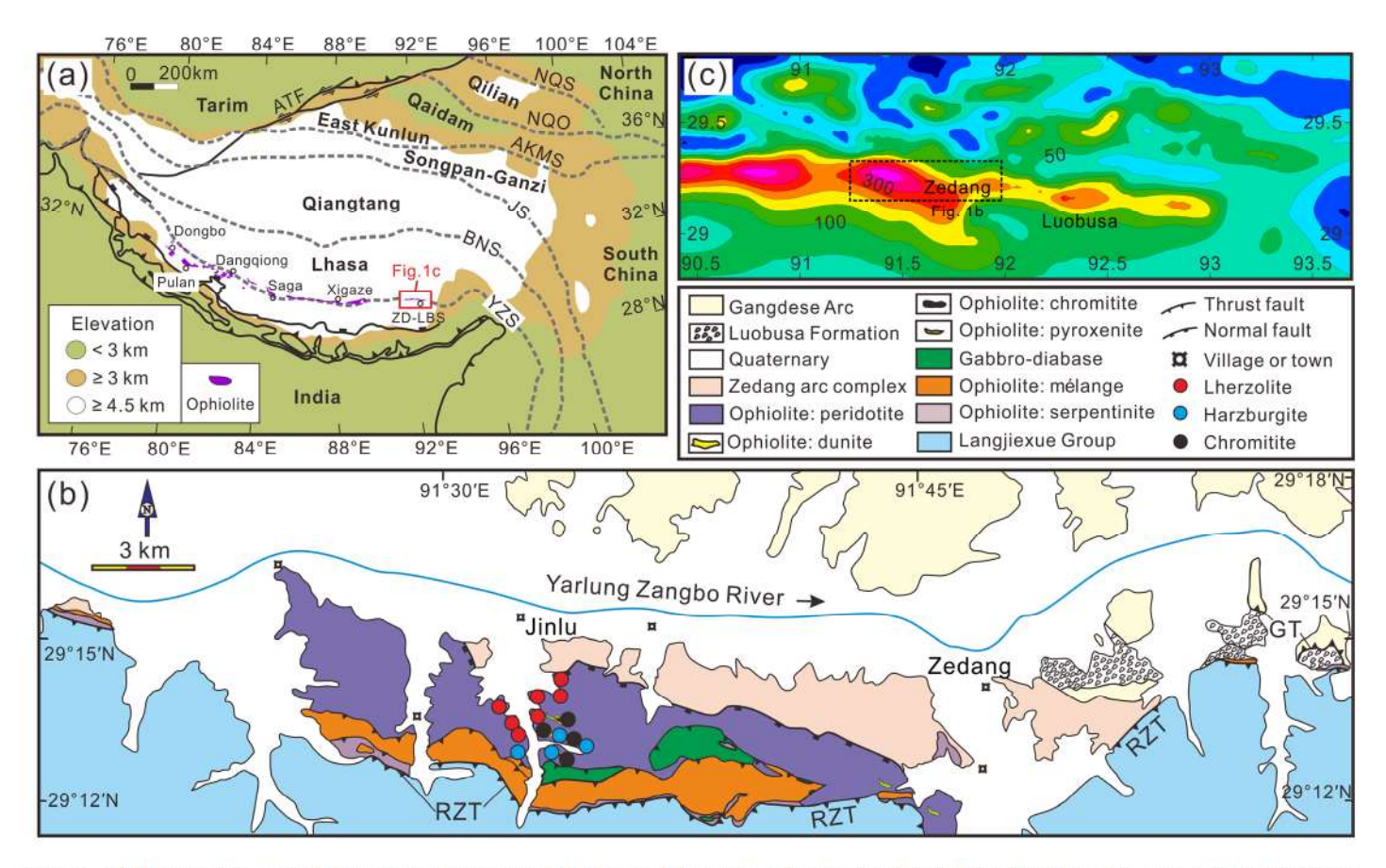


Figure 1. (a) Major tectonic units of the Tibetan Plateau and the location of the Yarlung-Zangbo ophiolite belt (modified after Dai et al., 2011; DeCelles et al., 2002). (b) Geological sketch map of the Zedang ophiolite and sampling locations (modified after McDermid et al., 2002; Xiong et al., 2017). (c) Regional aeromagnetic anomalies at the Zedang area (modified after Jiang et al., 2013). The contour interval is 50 nT. Abbreviations: YZS, Yarlung-Zangbo suture; BNS, Bangong-Nujiang suture; JS, Jinsha suture; AKMS, Anyimaqen-Kunlun-Muztagh suture; NQO, North Qaidam orogen; NQS, North Qilian suture; ATF, Altyn Tagh fault; GT, Gangdese thrust; RZT, Renbu-Zedang thrust.

2. Geological Setting

The Yarlung-Zangbo ophiolites in southern Tibet represent the lithospheric residues of the Neo-Tethys Ocean. The Zedang ophiolite covers an area of ~50 km² in the eastern part of the belt (Figure 1b). The ophiolite is sandwiched between the Zedang arc complex in the north and Triassic flysch in the south. The peridotite massif is composed of mainly harzburgite and lherzolite with minor dunite-chromitite veins. Dolerite dykes intruded the peridotite body and yield zircon crystallization ages of ~130 Ma (Xiong et al., 2016), consistent with the widespread mafic magmatism in the Yarlung-Zangbo ophiolite belt during early Cretaceous times (Wu et al., 2014). The Zedang ophiolite generates strong aeromagnetic anomalies of 150–350 nT (Figure 1c). The anomalies spread along the ophiolite body and extend to the west due to possibly some unexposed ultramafic terrains (Jiang et al., 2013, 2016). Serpentinized peridotite with magnetite precipitation has been proposed as the magnetic origin of the anomalies (He et al., 2014), but the magnetic and petrological signatures of serpentinization and magnetite formation are not well understood.

3. Methods

3.1. Magnetic Measurements

The samples used for magnetic measurements are mainly variably serpentinized peridotites but also include minor dolerite, chromitite, and volcanic rocks. Density (ρ) and magnetic susceptibility (K) were measured using fresh cores (1-2 cm in diameter) with a Sartorius balance (BT423S, 0.001 g) with density

LI ET AL. 2 of 15

Table 1 Density	1 and Magn	etic Param	reters of Se	erpentinize	Ta ble 1 Density and Magnetic Parameters of Serpentinized Peridotites of the Zedang Ophiolite, SE Tibet	e Zedang O	phiolite, SE	? Tibet									
Sample		Lithology ($(g cm^{-3})$	κ 10 ⁻⁶ (SI)	$(10^{-8} \frac{\chi}{m^3} \text{ kg}^{-1})$	(Am^{-1})	$NRM (Am^{-1})$	Q_n	$M_{\rm s}(10^{-3} { m Am2 kg}^{-1})$	$M_{\rm rs}(10^{-3}{ m Am}^2{ m kg}^{-1})$	$\frac{B_c}{(\mathrm{mT})}$	B_{cr} (mT)	B_{cr}/B_{c}	M_{rs}/M_s	$(10^{\frac{\kappa_{pgarq}}{198}} \frac{\%}{\text{kg}})$	mt (wt%)	8 (%)
10ZD-6-1		herzolite	3.262	1,670		0.07	0.72	4,50,00	52.18	7.05	15.58	34.50	2.21	0.14	14.3	90.0	5.0
10ZD-6-7	7	herzolite	3.108	17,397	559.68	89.0	1.76	2.7	624.45	89.15	17.46	36.13	2.07	0.14	6.6	89.0	26.2
10ZD-6-9	~	herzolite	3.281	4,403	134.22	0.17	1.25	7.7	144.76	24.10	21.98	46.80	2.13	0.17	13.7	0.16	2.8
10ZD-6-10		Cherzolite	3.162	006'6	313.08	0.39	6.04	16.5	304.41	53.57	22.50	40.90	1.82	0.18	13.5	0.33	18.4
10ZD-6-13	-	Lherzolite	3.281	2,488	75.84	0.10	2.31	25.0	133.60	23.81	27.54	54.00	1.96	0.18	14.0	0.15	2.8
10ZD-6-15		Cherzolite	3.272	3,930	120.10	0.15	0.17	1.2	172.42	32.40	25.16	53.36	2.12	0.19	15.4	0.19	4.0
10ZD-6-16	77.	Lherzolite	3.239	6,629	204.64	0.26	0.49	2.0	373.13	52.25	16.96	33.95	2.00	0.14	12.9	0.41	8.7
10ZD-6-18	-	Lherzolite	3.286	3,092	94.10	0.12	2.12	18.5	183.55	23.78	19.68	41.29	2.10	0.13	11.9	0.20	2.3
10ZD-6-19		Lherzolite	2.917	30,836	1057.23	1.20	12.4	10.9	1256.59	120.23	9.91	22.80	2.30	0.10	10.5	1.37	52.9
10ZD-6-20	3 8	Lherzolite	3.254	4,266	131.09	0.17	0.14	6.0	74.67	8.80	13.41	26.78	2.00	0.12	14.2	80.0	0.9
10ZD-6-3		Harzburgite	3.308	932	28.17	0.04	0.51	14.7	14.13	1.90	15.09	36.66	2.43	0.13	14.8	0.02	0.0
10ZD-6-5	*	Harzburgite	3.308	1,576	47.66	90.0	0.05	8.0	39.66	5.43	10.31	17.99	1.75	0.14	13.7	0.04	0.0
10ZD-6-6		Harzburgite	2.784	23,907	858.74	0.93	0.27	0.3	828.71	127.23	15.55	32.16	2.07	0.15	19.4	0.90	68.5
10ZD-6-17		Harzburgite	3.316	106	27.17	0.04	2.15	9.49	30.82	4.76	13.58	28.30	2.08	0.15	15.4	0.03	0.0
10ZD-4-4		Harzburgite	2.593	20,253	781.04	0.79	1.45	1.9	1128.92	157.00	14.58	35.25	2.42	0.14	0.9	1.23	94.2
15ZD-01		Harzburgite	3.055	16,590	543.13	0.65	1.46	2.4	663.36	77.80	13.08	32.25	2.46	0.12	11.4	0.72	33.3
15ZD-02		Harzburgite	3.195	4,681	146.49	0.18	0.34	2.0	345.24	30.52	12.26	29.87	2.44	60.0	10.1	0.38	14.3
15ZD-03		Harzburgite	2.613	24,495	937.48	96.0	4.88	5.4	1317.88	137.64	10.72	23.42	2.18	0.10	3.3	1.43	92.3
15ZD-04		Harzburgite	2.842	28,801	1013.43	1.12	0.52	0.5	1931.23	227.73	14.95	33.07	2.21	0.12	4.2	2.10	8.49
15ZD-05		Harzburgite	3.202	7,007	218.82	0.27	0.13	0.5	557.13	78.03	17.69	38.76	2.19	0.14	11.4	0.61	14.0
15ZD-06		Harzburgite	3.219	7.115	221.05	0.28	0.12	0.5	433.65	76.97	17.24	34.83	2.02	0.18	14.7	0.47	11.5

Note. ρ , density, κ , volume susceptibility; χ , mass susceptibility; J_i , induced magnetization; NRM, natural remanent magnetization; Q_i , Köenigsberger ratio (= NRM/ J_i , SI). M_s , saturation magnetization; M_{rs} , saturation remanence; B_c , coercivity; B_{cs} coercivity of remanence; κ_{para} , paramagnetic susceptibility; m_t , weight percent of magnetite; S_i , the degree of serpentinization.

LI ET AL. 3 of 15

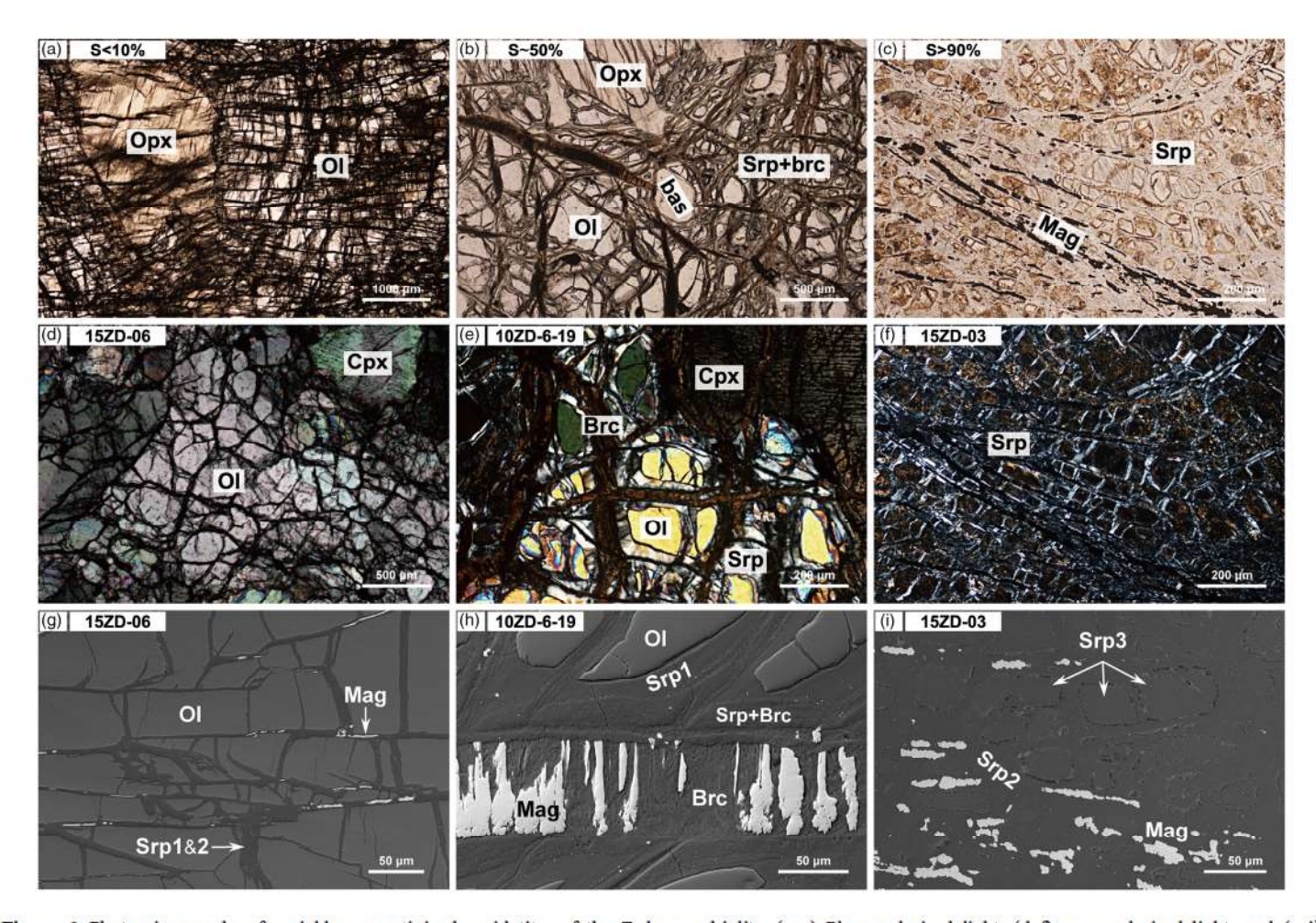


Figure 2. Photomicrographs of variably serpentinized peridotites of the Zedang ophiolite. (a–c) Plane-polarized light, (d–f) cross-polarized light, and (g–i) backscattered electron image. The degree of serpentinization (S) < 10% (a, d, and g), ~50% (b, e, and h), and >90% (c, f, and i). Ol, olivine; Opx, orthopyroxene; Cpx, clinopyroxene; Bas, bastite; Srp, serpentine; Brc, brucite; Mag, magnetite.

determination kit and an AGICO Kappabridge KLY-3s respectively at the China University of Geosciences (CUG, Wuhan). Natural remanent magnetization (NRM) was measured using the same core specimens with an AGICO JR-6A spinner magnetometer at the China Earthquake Administration (CEA, Beijing). Magnetic hysteresis, temperature dependence of susceptibility, and low-temperature remanence were carried out at the Institute for Rock Magnetism (IRM), University of Minnesota, USA. Magnetic hysteresis loops, backfield remanence curves, and first-order reversal curves (FORCs) were measured at room temperature on small core pieces using a Princeton VSM Model 3900 vibrating sample magnetometer (applied saturation field was 1.0 T).

Powder samples ($<250~\mu m$), crushed in an agate mortar, were used for thermomagnetic analysis. Magnetic susceptibility-temperature (K-T) experiments were conducted on a Kappabridge MFK1-FA from room temperature to 700°C in flowing argon gas. Low-temperature remanence (LTSIRM) curves were obtained using a Quantum Design MPMS-5S superconducting susceptometer between 20 and 300 K and follow the FC-ZFC-LTSIRM-RTSIRM LTD measurement protocol from Bilardello and Jackson (2013).

3.2. Mineralogical Analyses

Mineral analyses were conducted on polished thin sections (~0.1 mm thick) at the State Key Laboratory of Geological Processes and Mineral Resources (GPMR) and School of Earth Sciences, CUG Wuhan. Backscattered electron (BSE) images were collected by a Zeiss Sigma 300 field emission scanning

LI ET AL. 4 of 15



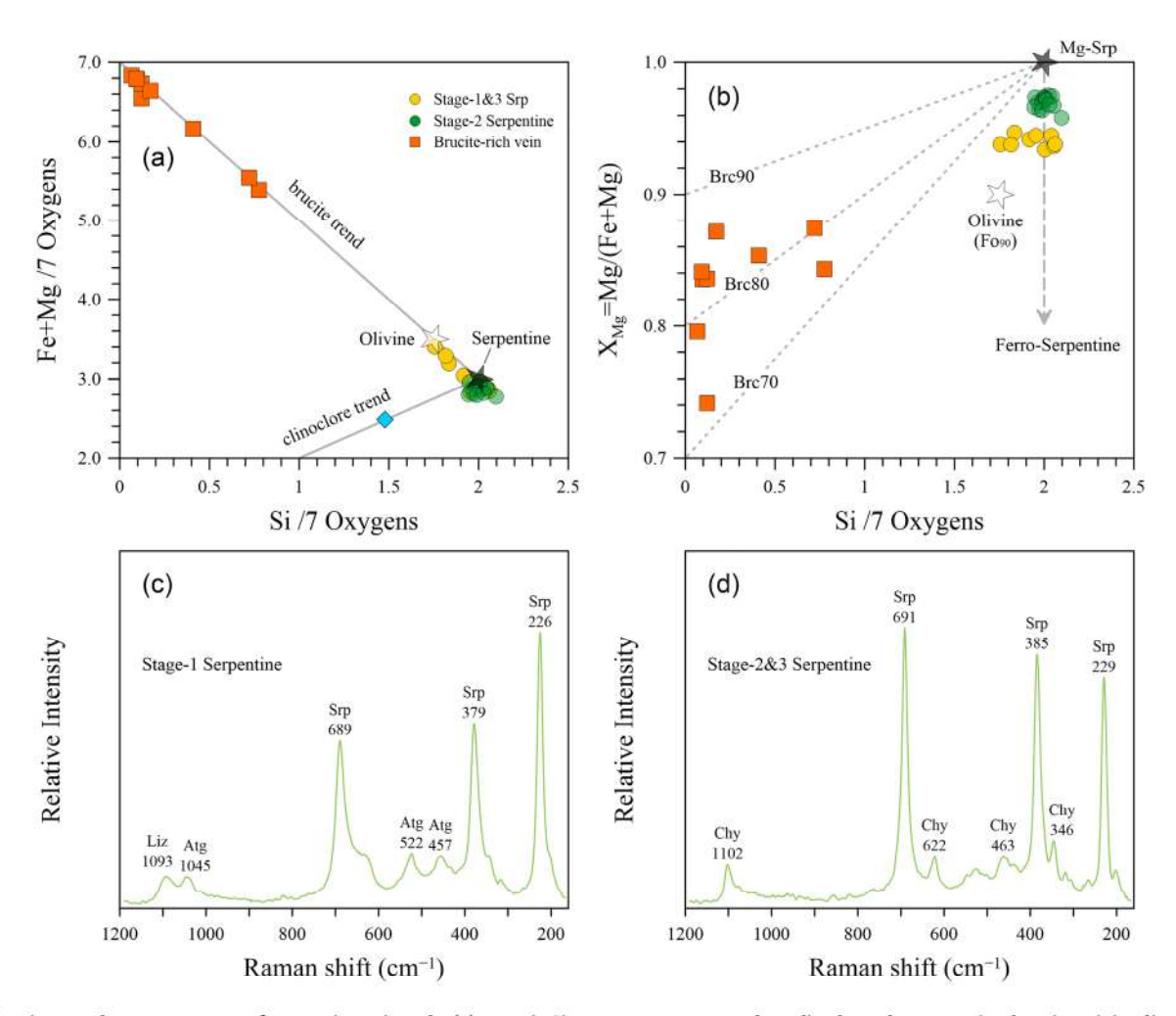


Figure 3. Chemistry and Raman spectra of serpentine minerals. (a) Atomic Si versus Fe + Mg. Analyses lie along the serpentine-brucite mixing line. (b) Si versus X_{Mg} . The Stage-1 and Stage-3 serpentines are more ferrous than Stage-2 serpentine (Srp). Brucite-rich mixtures (<50% Srp) show low X_{Mg} values from 0.7 to 0.9. (c) Stage-1 serpentine is largely a mixture of antigorite and lizardite. (d) Stage-2 and Stage-3 serpentines are more like chrysotile. Typical peaks of antigorite (Atg, 520 cm⁻¹, 1,044 cm⁻¹), lizardite (Liz, 1,096 cm⁻¹), and chrysotile (Chy, 345 cm⁻¹, 620 cm⁻¹, 1,105 cm⁻¹) refer to Rinaudo et al. (2003) and Groppo et al. (2006).

electronic microscope equipped with Oxford Instruments energy dispersive spectrometers. Raman spectra of serpentine minerals were obtained using a Thermo Scientific DXR dispersive microspectrometer with a 532 nm laser source. The chemical compositions of minerals were analyzed using a JEOL JXA-8230 electron probe microanalyzer (EPMA) with four wavelength dispersive spectrometers. The operating conditions are 15 kV accelerating voltage, 20 nA probe current, and a beam diameter of $1-3~\mu m$. A total of 11 major elements were measured for each mineral and standard minerals from SPI (USA) were utilized to determine the compositions (Wang et al., 2019). Dwell times were tens on element peaks and half that on background locations adjacent to peaks. Raw X-ray intensities were corrected using a ZAF (atomic number, absorption, and fluorescence) correction procedure (Armstrong, 1991).

4. Results

4.1. Petrography and Serpentine Mineralogy

The peridotite samples studied here are mainly harzburgites and lherzolites with densities (ρ) from 3.316 to 2.593 g cm⁻³ (Table 1), equivalent to 0–94% of the degree of serpentinization (S) estimated using a magnetite-weight corrected empirical equation: $S(\%) = (3.3 - [(\rho - 5.2 \times \text{mt\%})/(1 - \text{mt\%})])/0.785 \times 100$

LI ET AL. 5 of 15

The mole per-

 Table 2

 EPMA Results of Minerals in Selected Serpentinized Peridotites of the Zedang Ophiolite, SE Tibet

		Srp3	1	43.39	p.q.	0.14	0.05	4.44	0.07	37.68	60.0	0.03	0.01	0.25	86.14	2.061		0.002	800.0		0.176	0.003	2.668	0.005	0.003	0.000	0.010	4.935	0.94			
	-03	Srp2	3	43.58	0.01	60.0	0.01	2.32	0.07	39.77	0.07	0.02	0.00	0.19	86.13	2.049	0.000	0.000	0.005		0.091	0.003	2.788	0.003	0.001	0.000	0.007	4.949	0.97			
	15ZD-03	Cr-Mt																		1.779						0.000		3.000			0.89	
		Mt	2	0.30	0.01	0.01	p.d.	92.59	0.03	0.13	p.q.	p.d.	0.00	p.d.	93.06	0.011	0.000		0.000	1.977	1.003	0.001	800.0			0.000		3.000			0.99	
		Brc	4	1.53	0.00	0.03	0.00	23.46	0.35	54.38	0.58	0.02	0.00	0.03	p.d.	0.102	0.000	0.000	0.002		1.311	0.020	5.416	0.042	0.002	0.000	0.002	868.9	0.81			86.0
		Srp-Brc							0.27										0.029		0.847		and s	956								0.79
		3rc-Srp S							0.10										0.040		0.207	0.004	3.136	0.002	0.000	0.001	0.015	5.193	0.94			0.20
	0ZD-6-19	Srp1 Bi							60.0												0.189	004	.730	.003	.002	000	.001	896	94			
	10ZI	~																														
		Srp/Op	2	41.06	0.01	2.38	0.55	3.21	0.09	37.48	0.10	0.03	p.d.	0.01	84.91	1.97	0.00	0.02	0.13		0.12	0.00	2.68	0.00	0.00		0.00	4.95	0.95			
Sample		Cr-Mt	1	1.03	0.12	0.77	10.48	80.32	0.40	1.42	p.q.	0.01	p.q.	p.q.	94.55	0.039	0.003	0.311	0.034	1.572	0.948	0.013	0.080		0.001			3.000		0.11	0.79	
		Mt	2	0.13	0.02	0.01	0.00	93.75	0.05	80.0	p.q.	p.d.	p.q.	p.q.	94.04	0.005	0.001	0.000	0.001	1.988	0.999	0.002	0.005					3.000			0.99	
		Srp/Opx	1	40.90	0.01	3.24	0.41	2.37	80.0	38.17	0.15	0.02	0.01	p.d.	85.36	1.945	0.000	0.016	0.182		0.094	0.003	2.706	0.008	0.001	0.001		4.957	76.0			
		Srp2	3	45.44	0.01	1.08	0.02	2.04	90.0	40.10	0.10	0.01	0.01	0.19	90.98	1.999	0.000	0.001	090.0		0.080	0.003	2.815	0.005	0.001	0.000	0.007	4.971	0.97			
	10ZD-6-7	Cr-Mt	2															22		821	-10		_		223			3.000			0.74	
		Mt	2	0.40	0.03	0.01	0.01	2.77	0.02	0.15	p.d.	0.01	0.00	p.d.	3.39	0.016	0.001	0.000	0.000	1.967	1.006	0.000	0.008		0.001	0.000		3.000			1.00	
		Sp																												0.19	0.02	-
		Srp2	4																													
	0ZD-6-18	Mt	2																									3.000			86.0	
	10Z	lo																										2.982				
															300															4 ⁴		
		Phase	n.	SiO ₂	TiO2	Al_2O_3	Cr_2O^3	FeOr	MnO	MgO	CaO	Na ₂ O	K20	OiN	Total	Si	F	Ü	Al	Fe ³⁺	Fe ²⁺	Mn	Mg	Ca	Na	X	ïZ	Sum	X _{Mg}	XFeCr20	XFe304	brc%c

^bThe mole fraction of end-members FeCr₂O₄ and Fe₃O₄. Note. Ol, olivine; Mt, magnetite; Srp, serpentine; Sp, spinel; Cr-Mt, Cr-magnetite; Brc, brucite. $^aX_{Mg} = Mg/(Mg + \Sigma Fe)$. bd., below detection. Single-spot analysis refers to Table S1 in the supporting information. centage of brucite in serpentine-brucite mixtures $(1 - (Si/Mg + Fe)_{measured}/0.67_{serpentine})$.

LI ET AL. 6 of 15

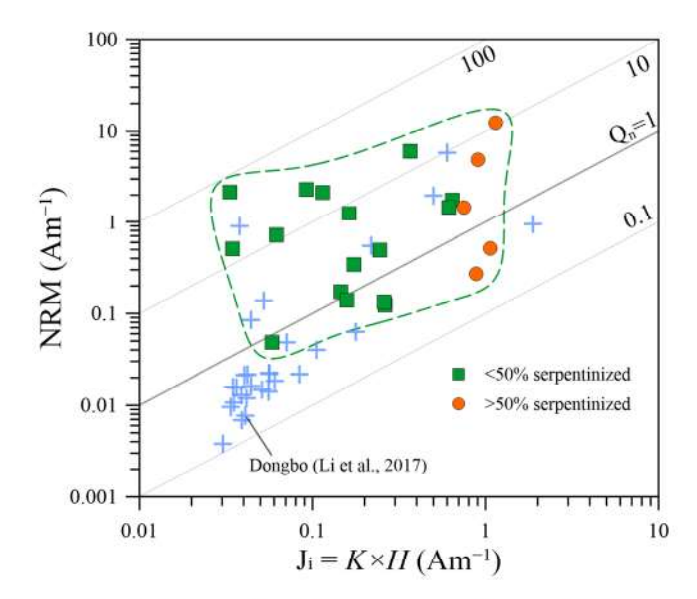


Figure 4. Plot of induced magnetization (J_i) versus natural remanent magnetization (NRM). The >50% serpentinized samples show higher induced magnetization than the <50% serpentinized samples. The Köenigsberger ratio Q_n equals to NRM/KH, where H is 37 Am $^{-1}$ for the local geomagnetic field in the Zedang area.

(Miller & Christensen, 1997; Oufi et al., 2002). The magnetite weight percent (mt%) was estimated from the bulk saturation magnetization (M_s) and the known values for pure magnetite (92 Am² kg⁻¹) as mt% = M_s sample/92 × 100% by assuming that magnetite (~5.2 g cm⁻³) is the only mineral contributing to saturation magnetization.

The occurrence of fresh minerals (olivine + orthopyroxene + clinopyroxene + spinel) has been described in detail by Xiong et al. (2017). The characteristics of serpentinization are similar for the two types of peridotite. Olivine has been progressively replaced by serpentine along cleavages and grain boundaries, forming typical mesh textures (Figures 2a–2f). Pyroxene (mostly orthopyroxene) was partly altered to bastite pseudomorphs with uniform extinction. Brucite veins are recognized by a characteristic reddish to brown color in samples that have experienced 50–70% serpentinization (Figure 2b). Magnetite was observed in all the samples with two typical modes of occurrence (Figures 2g–2i). Magnetites in the serpentine veins are fine-grained and spread parallel to the veins. By contrast, magnetite grains in the brucite veins arrange in grid-like shape and are perpendicular to the vein boundaries.

The serpentine veins are divided into three stages. Stage-1 serpentine (Srp1) directly contacts with olivine and does not contain any magne-

tite (Figure 2h). Srp1 is separated from central brucite-magnetite veins by a narrow band of serpentine-brucite intergrowths. Stage-2 serpentine (Srp2) contains magnetite grains or veins and shows no signature of brucite (Figure 2i). Stage-3 serpentine (Srp3) replaced the mesh center olivine and is free of magnetite (Figure 2i). Mineral chemistry results show that the serpentine minerals mainly follow the serpentine-brucite mixing line (Figure 3a). The Stage-1 and Stage-3 serpentines contain somewhat more FeO (3.92–5.12 wt%, $X_{\rm Mg} \sim 0.94$) than Stage-2 serpentine (FeO = 1.84–2.88 wt%, $X_{\rm Mg} \sim 0.97$) (Table 2 and Figure 3b), where $X_{\rm Mg} = {\rm Mg/(Mg + Fe)}$. The brucite (containing <10% Srp) and brucite-rich mixtures (<50% Srp) show lower $X_{\rm Mg}$ values from 0.74 to 0.87. Raman spectra analyses suggest that the Stage-1 serpentine is likely a mixture of antigorite (typical peak at 1,045 cm⁻¹) and lizardite (1,093 cm⁻¹) while the Stage-2 and Stage-3 serpentines are largely chrysotile (1,102 cm⁻¹, 620 cm⁻¹) (Figures 3c and 3d).

4.2. Magnetic Susceptibility and NRM Intensity

Magnetic susceptibility (K) and NRM intensity values are summarized in Table 1. The susceptibility increases from <0.001 to ~0.02 SI for the S < 50% samples and ranges from 0.02 to 0.03 SI for the S > 50% samples. The NRM intensity varies broadly from 0.05 to 12.4 Am $^{-1}$ for all samples and lacks trend with increasing serpentinization. Some slightly serpentinized samples (S < 10%) have remarkably high NRM of up to 2.31 Am $^{-1}$. The maximum susceptibility and NRM are from one ~50% serpentinized sample (10ZD-6-19), which contains many brucite-magnetite veins (Figure 2). The Köenigsberger ratio (Q_n = NRM/KH, where H is 37 Am $^{-1}$ for the local geomagnetic field) varies between 0.3 and 64.6. More than two thirds of the samples have Q_n values >1, suggesting that remanent magnetization prevails over induced magnetization in these rocks. The remaining samples have Q_n values <1 and thus are dominated by induced magnetization (Figure 4).

4.3. Identification of Main Ferrimagnetic Phases

Thermomagnetic analyses and electron probe microanalyses have been utilized to determine the ferrimagnetic phases. Pure magnetite (Curie temperature, $T_c \sim 585^{\circ}\text{C}$) is identified by the K-T curves for all the selected samples with variable degrees of serpentinization (Figures 5a–5d). Magnetite (Verwey transition, $T_v \sim 120~\text{K}$) is also the major remanence carrier as shown by the FC and ZFC warming curves, and low-temperature cycling of RTSIRM (Figures 5e–5l). In addition, a weak T_c of 610–620°C on the K-T curves and the hump-shaped RTSIRM cycling below room temperature indicate the presence of minor amounts of oxidized magnetite (or maghemite) in the samples (Özdemir & Dunlop, 2010). Moreover, moderately serpentinized peridotites (S = 25–50%) show an additional ferrimagnetic phase with Curie temperatures of

LI ET AL. 7 of 15

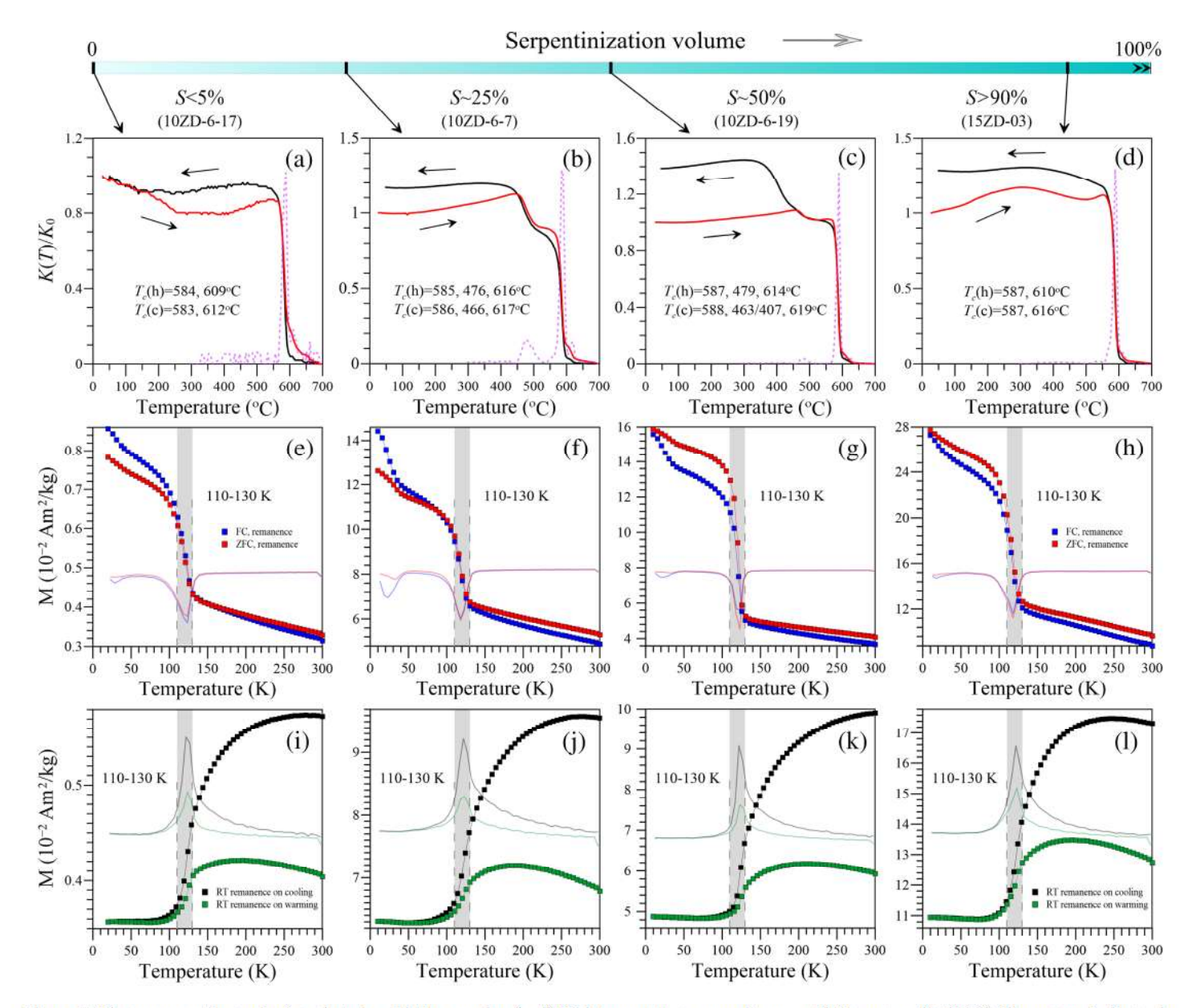


Figure 5. Thermomagnetic results for selected peridotite samples. (a–d) High-temperature magnetic susceptibility curves (0–700°C). The arrows indicate the heating (red) and cooling (black) directions. The Curie temperature $T_c(h)$ and $T_c(c)$ were estimated from the peak of the first derivative of smoothed heating and cooling curves. (e–l) Low-temperature magnetic measurements (0–300 K): (e–h) field cooled (FC, 2.5 T) and zero field cooled (ZFC) remanence warming curves; (i–l) cooling-warming curves of 2.5 T room temperature saturation isothermal remanent magnetization (RTSIRM). The transition at T=110-130 K corresponds to the Verwey transition temperature of magnetite.

400–500°C (Figures 5b and 5c). This phase is possibly Cr-magnetite, which occurs as alteration rims around relic spinels (Figure S1 in supporting information). Similar occurrences have been found in the Dongbo ophiolite in the eastern part of the Yarlung-Zangbo suture (Li et al., 2017) as well as other ophiolitic serpentinites (e.g., Hodel et al., 2017).

Chemical composition analyses of the iron oxides (Table 2) are consistent with the thermomagnetic results. Magnetite contains 0.97–1.0 mole fractions of Fe_3O_4 endmember (X_{Fe3O4}) with minor amounts of MgO and SiO_2 (<1.5 wt%). The Cr-magnetite rims show varying compositions of FeO (76.4–80.3 wt%) and Cr_2O_3 (10.5–14.0 wt%). Particles that contain 0.74–0.79 X_{Fe3O4} correspond to K-T curves exhibiting the lower $T_c = 400$ –500°C phase (Figures 5b and 5c).

LI ET AL. 8 of 15

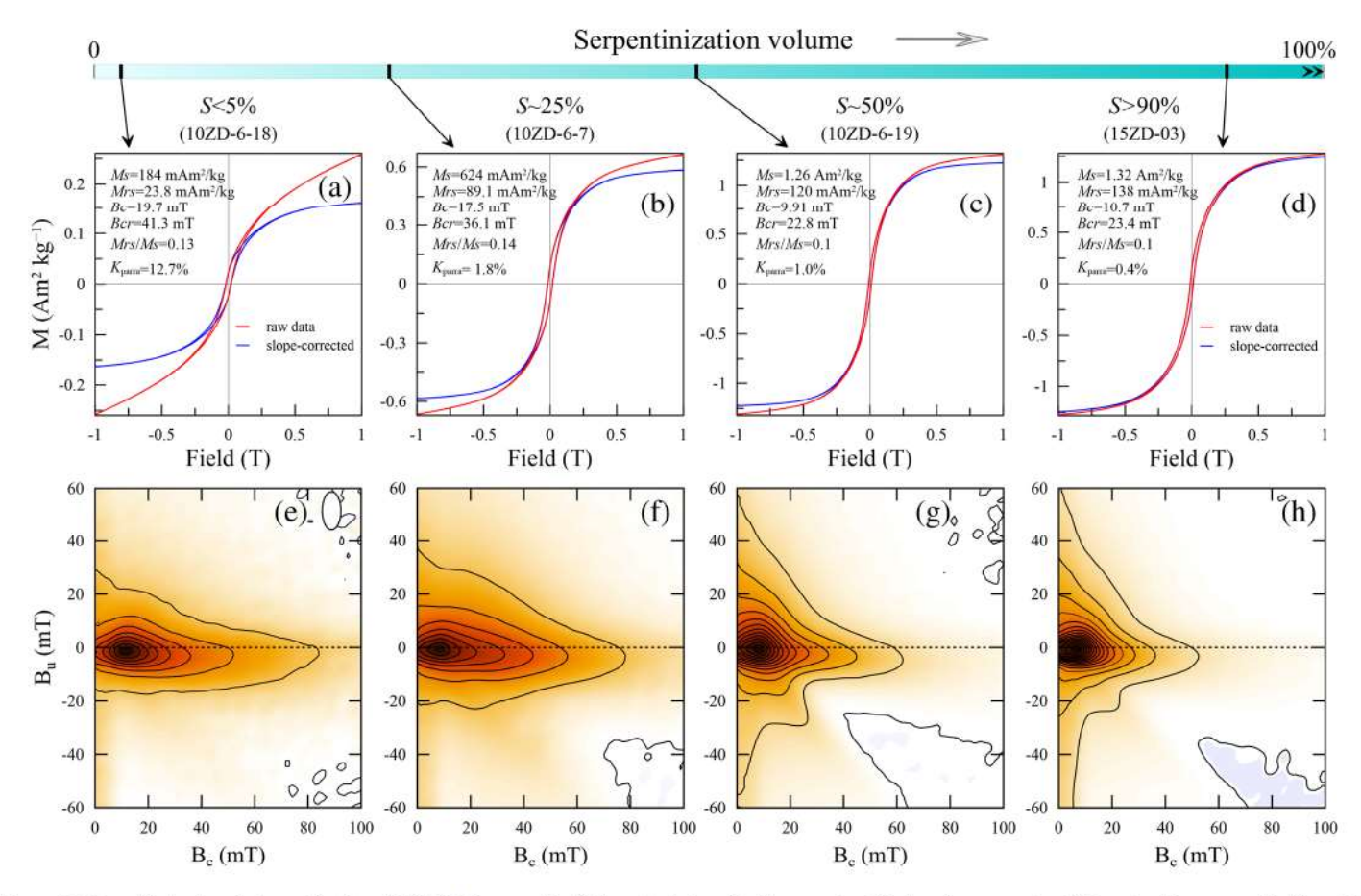


Figure 6. Magnetic hysteresis loops (a-d) and FORC diagrams (e-h) for selected peridotite samples. Hysteresis parameters (M_s , saturation magnetization; M_{rs} , saturation remanence; B_c , coercivity) are calculated after paramagnetic slope correction over the interval of 0.7–1.0 T using the nonlinear approach-to-saturation fitting method (Jackson & Solheid, 2010). Coercivity of remanence (B_{cr}) is determined from DC backfield remanence curve. Paramagnetic susceptibility (K_{para}) is from the high field (>0.7 mT) slope correction. FORCs (104 curves per sample) are processed using FORCinel 3.0 (Harrison & Feinberg, 2008) with drift correction, first/last point replacement, lower branched subtraction (10 FORCs), and a smoothing factor of 5.

4.4. Magnetic Hysteresis and FORCs

All the peridotite samples display ferrimagnetic hysteresis loops regardless of the degree of serpentinization (Figures 6a–6d). Magnetic hysteresis parameters after paramagnetic slope corrections are summarized in Table 1. The paramagnetic susceptibility contribution (K_{para} , mainly from silicates), from high field slope calculation (>0.7 T), decreases from 56.5% to 0.4% with progressing serpentinization from S < 5% to > 90%, suggesting an increase of ferrimagnetic mineral abundance (essentially magnetite). As magnetite dominates the ferrimagnetic phases (from K-T results), M_s constitutes a proxy for the concentration of magnetite (e.g., Bina & Henry, 1990; McCollom et al., 2016; Oufi et al., 2002). The Zedang samples show M_s values ranging from 14 to 1931 \times 10⁻³ Am² kg⁻¹, indicating wt% magnetite from 0.02% to 2.1% (Table 1).

The M_{rs}/M_s and B_{cr}/B_c values vary from 0.09 to 0.2 and from 1.75 to 2.5, respectively (Table 1). While there is ambiguity in interpreting M_{rs}/M_s - B_{cr}/B_c data (Heslop & Roberts, 2012; Roberts et al., 2019), the Zedang samples plot in the pseudo-single-domain (PSD) field (Figure S2 in the supporting information) and follow the theoretical trends for mixtures of single-domain (SD, 0.03–0.1 μ m) and multidomain (MD, >20 μ m) magnetite (Day et al., 1977; Dunlop, 2002; Tauxe et al., 2002). This is confirmed by the FORC diagrams (Figures 6e–6h) that show samples are dominated by PSD/MD particles. The coercivity peaks at 5–20 mT and FORC contours extending along the horizontal axis are signatures of higher coercivity (possibly SD), finer-grained magnetite particles, whereas the divergent outer contour lines with vertical distributions are more typical of PSD to MD particles (Pike et al., 2001; Roberts et al., 2014). Additionally, the S < 50% samples show FORC diagrams consistent with finer-sized SD/PSD particles (Figures 6e–6f) while the FORC

LI ET AL. 9 of 15

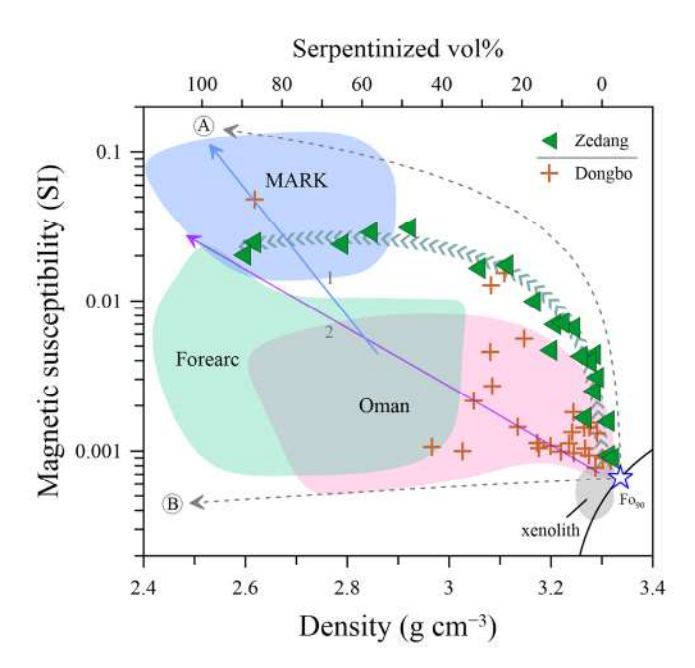


Figure 7. Density-magnetic susceptibility relationships for various serpentinized peridotites. The path (A) predicts maximum magnetite and (B) no magnetite formation in the serpentinization reactions of olivine (Fo₉₀) (Toft et al., 1990). Lines 1 and 2 are fitted trends for abyssal (Oufi et al., 2002) and ophiolite samples (Toft et al., 1990), respectively. The data/fields of the Dongbo ophiolite (Li et al., 2017), the Oman/Pindos ophiolites (Bonnemains et al., 2016), the MARK ODP 153 samples (Klein et al., 2014; Oufi et al., 2002), the Mariana forearc samples (Salisbury et al., 2002; Stokking et al., 1992), and mantle xenoliths (Ferré et al., 2013; Li et al., 2015) are shown for comparison.

diagrams for S>50% samples are consistent with coarser-sized PSD/MD particles (Figures 6g–6h). The FORC and hysteresis results are also consistent with the low-temperature remanence curves (Figures 5e–5h) where samples with S>50% have ZFC remanence greater than the FC remanence below the Verwey transition (T<120 K) and is an indicator for MD particles (Carter-Stiglitz et al., 2006). The opposite behavior is observed for S<50% characteristic for finer sized SD particles.

5. Discussion

5.1. Density-Magnetic Susceptibility Relationship

As magnetite is the dominant magnetic carrier in serpentinized peridotites, higher magnetic susceptibilities generally indicate a higher content of magnetite. Therefore, the density-magnetic susceptibility (D-K) relationship has been used to evaluate the formation of magnetite during the scrpentinization (Figure 7). Samples of the western Cordillera ophiolites (Josephine, Burro & Red Mountains) form a linear D-K trend that starts at fresh mantle, but the susceptibility values at low degrees of serpentinization were lower than predictions for typical reactions that produce magnetite (Toft et al., 1990). In addition, a rapid increase of magnetic susceptibility at > ~60-70% serpentinization was observed for abyssal peridotites (e.g., ODP 153 in the Mid-Atlantic Ridge at Kane, MARK area) (Oufi et al., 2002) and the Mirdita ophiolite (Albania) (Maffione et al., 2014), suggesting that magnetite is mainly produced in the late stages of serpentinization. However, for the Oman (mainly the Fizh block) and Pindos (Greece) ophiolites (Bonnemains et al., 2016), as well as the Mariana forearc (ODP 125 and ODP 195) (Klein et al., 2014), serpen-

tinized peridotites show very low magnetic susceptibility and magnetite content in almost the entire process of serpentinization (Bonnemains et al., 2016; Klein et al., 2014).

An earlier study of the Dongbo ophiolite in the western Yarlung-Zangbo suture zone (Li et al., 2017) showed that the S < 50% peridotites mainly have comparable magnetic susceptibilities to the Oman/Pindos and forearc samples (Figure 7). For the Zedang peridotites, the S < 50% samples show susceptibilities from <0.001 to ~0.02 SI, which increase following the predicted trend for serpentinization that is coupled with magnetite formation (Toft et al., 1990). The values are slightly higher than those of the Dongbo, Oman/Pindos ophiolites, and forearc peridotites, indicating a relatively higher content of magnetite in the Zedang samples. However, for the S > 50% samples, the magnetic susceptibility becomes nearly constant at 0.02–0.03 SI instead of increasing to higher values as found for many abyssal peridotites (Bach et al., 2006; Oufi et al., 2002). The Zedang peridotites present a curvilinear, upward pathway of magnetic susceptibility with progressive serpentinization (Figure 7), which differs from the other groups as mentioned above and suggests a limit of magnetite formation after ~50% serpentinization.

5.2. The Conditions of Serpentinization and Magnetite Formation

The serpentinization process in natural systems is complex and characterized by multiple reaction paths and stages depending on the conditions such as fluid/rock ratio, silica activity, and temperature. Bach et al. (2006) proposed a two-step model of early hydration of olivine to form serpentine and Fe-rich brucite in a rock-dominated closed system followed by Fe-rich brucite reacting with aqueous silica and formation of serpentine and magnetite in a fluid-dominated open system. The Zedang peridotites contain fine-grained magnetite and Fe-poor serpentine mesh (2–3 wt% FeO) at low degrees of serpentinization (S < 50%) (Figure 2 and Table 2), suggesting that the magnetite formation stage began shortly after the magnetite-free hydration occurred (Beard et al., 2009). This is consistent with the increasing trend of magnetic susceptibility, which follows the trend for coupled serpentinization and magnetite formation (Figure 7). However, at higher degrees of serpentinization (S > 50%), the olivine cores were replaced by Fe-rich serpentine (4–5 wt%)

LI ET AL. 10 of 15

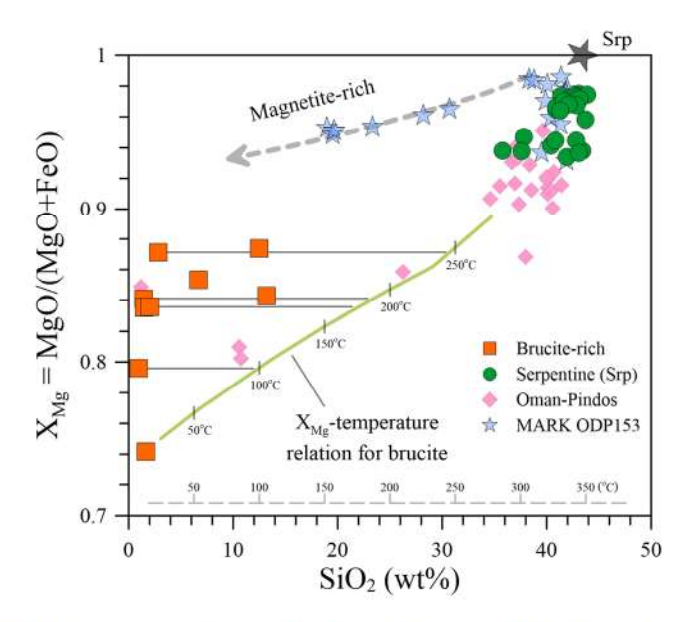


Figure 8. SiO_2 - X_{Mg} relationship for serpentine-brucite intergrowths. The magnetite-rich trend for MARK ODP 153 samples is from Klein et al. (2014). The X_{Mg} -temperature relationship for brucite (Klein et al., 2013) is shown to estimate serpentinization temperatures. The temperature axis (0–400°C) has no corresponding relationship to the SiO_2 axis. The orange squares refer to serpentine-brucite mixtures with >50% brucite (Brc and Srp-Brc in Table 2). Only those data containing >95% brucite were used for temperature estimate (denoted by thin lines linking to the X_{Mg} -temperature relationship from Klein et al., 2013). The data of Oman/Pindos ophiolites are from Bonnemains et al. (2016) and Mayhew et al. (2018).

FeO) without magnetite formation (Figure 2), and this causes the nearly horizontal portion of magnetic susceptibility versus density trend in the Zedang ophiolite on the *D-K* plot (Figure 7).

In previous studies, serpentinized peridotites that contain abundant magnetite (e.g., the Chenaillet ophiolite and MARK samples) were supposed to be formed at higher temperatures (>200-300°C), whereas magnetite-poor samples (e.g., the Oman/Pindos ophiolites) were formed at lower temperatures (<200-220°C) (Bonnemains et al., 2016; Klein et al., 2014; Mayhew et al., 2018). The Oman/Pindos samples also show more iron in serpentine than the MARK samples (Figure 8). The iron content in serpentines in the Zedang peridotites is in between the Oman ophiolite and MARK samples, which may represent an "in between" scenario of intermediate-temperature serpentinization. However, the brucite-serpentine and brucite-magnetite veins occur in the $S \sim 50-70\%$ samples (Figure 2). According to the model by Klein et al. (2013), the Fe content of brucite (X_{Me}) increases with the decrease of serpentinization temperature. The brucite (>90% brc) in the Zedang peridotite samples shows X_{Mg} values from 0.74 to 0.87 and indicates serpentinization temperatures from ~250 to <100°C (Figure 8). The presence of brucite veins above ~50% of serpentinization marks low silica activity (Frost & Beard, 2007) but also indicates that the earlier serpentinization (S < 50%) may take place at higher temperatures of >250-300°C as brucite is almost never produced above 300°C (Marcaillou et al., 2011; McCollom & Bach, 2009). In addition, the absence of brucite in the S > 90% samples (Figure 2) is likely due to the fact that brucite reacts with SiO2(aq) from the hydration of pyroxene or modified seawater and forms iron-rich scrpentine (Alt & Shanks, 2003; Bach et al., 2006; Huang et al., 2017).

Li et al. (2017) reported that the Dongbo peridotite samples (S < 50%) in the western part of the Yarlung-Zangbo ophiolite belt mainly have weak magnetization compatible with the Oman/Pindos samples (Bonnemains et al., 2016). By contrast, the Zedang ophiolite peridotites show magnetic and petrological characteristics compatible with high-temperature serpentinization ($>200-300^{\circ}\text{C}$) in the S < 50% stage and low-temperature serpentinization ($< \sim 200^{\circ}\text{C}$) in the S > 50% stage. These discrepant results could be explained by complex serpentinization histories and different thermal regimes depending on the original lithosphere architecture, as observed in other sample groups (e.g., Andreani et al., 2007; Bach et al., 2006; Oufi et al., 2002). Geochemical studies suggest that the Zedang peridotites were formed in multiple periods of modification and accretion in both spreading ridge and subduction forearc settings between the Neo-Tethyan slab and the Lhasa Block from ~ 200 to 55 Ma (e.g., Xiong et al., 2016, 2017). In this case, the Zedang samples may record serpentinization processes that started at a hot oceanic spreading ridge center, when the mantle was tectonically exposed to seawater, and subsequently progressed in near-seafloor settings with significant cooling of the lithosphere, possibly associated with ophiolite emplacement. However, the serpentinization history of the Yarlung-Zangbo ophiolites along the entire suture zone need further studies to understand these processes completely.

5.3. Magnetic Source in the Yarlung-Zangbo Ophiolites

To evaluate the source of aeromagnetic anomalies in the Yarlung-Zangbo ophiolites, the induced magnetization and NRM of several typical rocks that are exposed in the Zedang ophiolite are directly added together to get a total magnetization intensity ($M_{\rm total}$). The value is a theoretical maximum due to the uncertainty of NRM directions, but this simplification facilitates a straightforward comparison of magnetization intensities between different sample groups (Table 3). Dolerites show the lowest total magnetization (0.01–0.1 Am⁻¹) with an average of ~0.03 Am⁻¹, whereas basaltic volcanic rocks have a wider range (0.02–2 Am⁻¹) and higher average value of ~0.25 Am⁻¹. Serpentinized peridotites show comparable $M_{\rm total}$ values to chromitites (0.1–10 Am⁻¹), and both have larger average values of 2–3 Am⁻¹ (Figure 9a). In addition, about half of the

LI ET AL. 11 of 15

 Table 3

 Summary of Rock Density and Magnetization Intensity for the Zedang Ophiolite and Other Selected Suites

Lithology	Location	Nums. (S)	$\rho(\mathrm{gcm}^{-3})$	$\kappa (10^{-6} \mathrm{SI})$	J_i (Am ⁻¹)	NRM (Am ⁻¹)	Q _n	$M_{\rm total} ({\rm Am}^{-1})$	Reference
Dolerite	Zedang ophiolite	6	2.88 (2.80-3.04)	440 (341–609)	0.02 (0.01-0.02)	0.01 (0-0.05)	0.5 (0-2.3)	0.03 (0.02-0.07)	This study
Balaltic	Zedang ophiolite	15	2.92 (2.79-3.07)	2,755 (506-20,413)	0.1 (0.02-0.76)	0.14 (0-1.38)	3.4 (0-36.6)	0.25 (0.02-1.42)	This study
volcanics									
Chromitite	Zedang ophiolite	12	4.02 (3.66-4.33)	4,483 (2,548-9,060)	0.17 (0.09-0.34)	2.8 (0.25-9.22)	18.2 (1.6-59.8)	2.97 (0.34-9.38)	This study
Serpentinized	Zedang ophiolite	5	2.75 (2.59-2.92)	25,659 (20,253-30,836)	0.95 (0.75-1.14)	3.91 (0.27-12.4)	1.6 (0.2-5.1)	4.85 (1.16-13.5)	This study
peridotite	eastern Tibet	(S > 50%)							
		16	3.23 (3.05-3.32)	5,786 (901-17,397)	0.21 (0.03-0.64)	0.21 (0.03-0.64) 1.24 (0.05-6.04)	4.9 (0.2-18.4)	1.45 (0.11-6.4)	This study
		(S < 50%)							
Serpentinized	Dongbo ophiolitea	27	3.2 (2.97-3.32)	2,495 (777-15,400)	0.1 (0.03-0.6)	0.37 (0-5.85)	1.9 (0.1-23.7)	0.46 (0.03-6.45)	Li et al. (2017)
peridotite	western Tibet	(S < 50%)							
Serpentinized	MARK ODP 153	105	2.73 (2.5-2.89)	83,619 (29,000-129,000) 2.42 (0.84-3.74) 12.0 (3.31-38.4) 4.95 (2.44-12.3) 14.4 (4.15-41.6)	2.42 (0.84-3.74)	12.0 (3.31-38.4)	4.95 (2.44-12.3)	14.4 (4.15-41.6)	Oufi et al. (2002)
peridotite	(Mid-Atlantic	(S > 50%)							
Serpentinized	ODP 125&195	56	2.61 (2.42-2.82)	4,897 (60-16,310)	0.14 (0-0.47)	0.25 (0.01-0.75)	4.9 (0.3-81)	0.4 (0.01-1.19)	Stokking
peridotite	(Mariana forearc) $(S > 50\%)$	(S > 50%)							et al. (1992) and
									Salisbury
									et al. (2002)

Note. S, the degree of serpentinization. ρ , density; κ , volume susceptibility; J_i , induced magnetization; NRM, natural remanent magnetization; Q_n , Köenigsberger ratio (= NRM/Ji, SI). M_{total} , sum a Dunite is not included for chromite as the main ferrimagnetic phase.

LI ET AL. 12 of 15

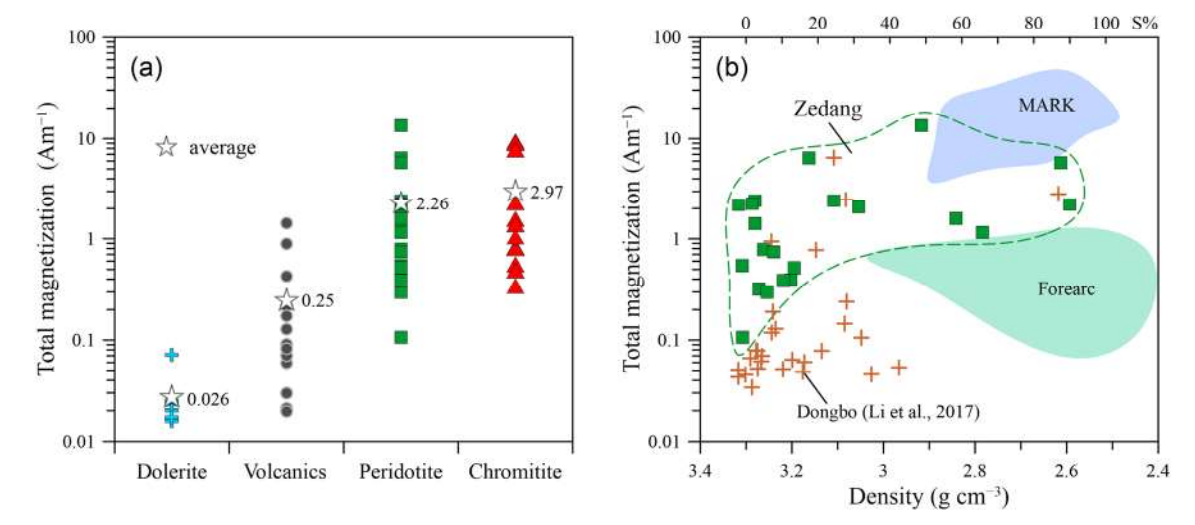


Figure 9. (a) Magnetization intensity of the Zedang ophiolite samples. The total magnetization equals to the sum of induced magnetization and natural remanent magnetization (NRM). (b) Plot of density versus magnetization for selected peridotite suites from different tectonic settings. The shaded areas are defined as the same in Figure 7, and the data references are listed in Table 3.

S < 50% and all the S > 50% peridotite samples of the Zedang ophiolite have intensities of 1–13.5 Am⁻¹ and partly overlap with the strongly magnetic MARK samples (4–45 Am⁻¹). The remaining S < 50% samples are weakly magnetic with lower $M_{\rm total}$ values (<1 Am⁻¹), similar to the Dongbo ophiolite (Li et al., 2017) and forearc samples (Figure 9b). Overall, most of the serpentinized peridotites are highly magnetized and should be a significant source of the aeromagnetic anomalies in the Zedang ophiolite and throughout the entire Yarlung-Zangbo suture zone (Jiang et al., 2016; Wang et al., 2020).

6. Conclusions

The magnetic and petrological properties of variably serpentinized peridotites from the Zedang ophiolite in southern Tibet were investigated and suggest that magnetite formation was prevented above \sim 50% serpentinization. The samples show a rapid increase of magnetic susceptibility before 50% serpentinization followed by nearly constant values above 50% serpentinization, which is consistent with the formation of Fe-poor serpentine mesh with magnetite in the early stages and Fe-rich serpentine cores without magnetite in the late stages. Brucite veins in the 50–70% serpentinized samples indicate serpentinization temperatures from \sim 250 to <100°C. The Zedang ophiolite may record serpentinization processes that started above 250°C at a hot oceanic spreading ridge axis and subsequently continued below 200°C in off-axis settings, possibly associated with ophiolite emplacement. The serpentinized peridotites show higher magnetization intensities than dolerite dykes and most basaltic volcanic rocks in the area and should mainly contribute to the aeromagnetic anomalies along the Yarlung-Zangbo suture in southern Tibet.

Acknowledgments

This study was supported by the National Natural Science Foundation of China (41504053, 41520104003, 41873032, and 41374094), the Fundamental Research Funds for the Central Universities (CUG180620), and the China Scholarship Council (201806415015). Mike Jackson at the IRM and Tao Yang at the CUG-Wuhan offered help with the magnetic measurements. We thank the Associate Editor Mark Dekkers and two reviewers who greatly improved the manuscript. This is IRM Contribution 2001. The IRM is supported by the Instruments and Facilities Program of the NSF Division of Earth Science.

Data Availability Statement

The magnetic data and mineral composition data presented in this paper can be accessed online (https://zenodo.org/record/3930567).

References

Aitchison, J. C., Badengzhu, D. A. M., Liu, J., Luo, H., Malpas, J. G., McDermid, I. R. C., et al. (2000). Remnants of a Cretaceous intra-oceanic subduction system within the Yarlung–Zangbo suture (southern Tibet). Earth and Planetary Science Letters, 183(1–2), 231–244. https://doi.org/10.1016/S0012-821X(00)00287-9

Alt, J. C., & Shanks, W. C. (2003). Serpentinization of abyssal peridotites from the MARK area, Mid-Atlantic Ridge: Sulfur geochemistry and reaction modeling. Geochimica et Cosmochimica Acta, 67(4), 641–653. https://doi.org/10.1016/S0016-7037(02)01142-0
Andreani, M., Mével, C., Boullier, A. M., & Escartín, J. (2007). Dynamic control on serpentine crystallization in veins: Constraints on hydration processes in oceanic peridotites. Geochemistry, Geophysics, Geosystems, 8, Q02012. https://doi.org/10.1029/2006GC001373

LI ET AL. 13 of 15



- Armstrong, J. T. (1991). Quantitative elemental analysis of individual microparticles with electron beam instruments. In K. F. J. Heinrich, & D. E. Newbury (Eds.), *Electron Probe Quantitation* (pp. 261–315). Boston, MA: Springer US. https://doi.org/10.1007/978-1-4899-2617-3_15
- Bach, W., Paulick, H., Garrido, C. J., Ildefonse, B., Meurer, W. P., & Humphris, S. E. (2006). Unraveling the sequence of serpentinization reactions: Petrography, mineral chemistry, and petrophysics of serpentinites from MAR 15°N (ODP Leg 209, Site 1274). Geophysical Research Letters, 33, L13306. https://doi.org/10.1029/2006GL025681
- Beard, J. S., Frost, B. R., Fryer, P., McCaig, A., Searle, R., Ildefonse, B., et al. (2009). Onset and progression of serpentinization and magnetite formation in olivine-rich troctolite from IODP Hole U1309D. *Journal of Petrology*, 50(3), 387–403. https://doi.org/10.1093/petrology/egp004
- Bilardello, D., & Jackson, M. (2013). What do the Mumpsies do? IRM Quarterly, 23(3), 1-15.
- Bina, M. M., & Henry, B. (1990). Magnetic properties, opaque mineralogy and magnetic anisotropies of serpentinized peridotites from ODP Hole 670A near the Mid-Atlantic Ridge. *Physics of the Earth and Planetary Interiors*, 65(1–2), 88–103. https://doi.org/10.1016/0031-9201(90)90078-C
- Blakely, R. J., Brocher, T. M., & Wells, R. E. (2005). Subduction-zone magnetic anomalies and implications for hydrated forearc mantle. Geology, 33(6), 445–448. https://doi.org/10.1130/G21447.1
- Bonnemains, D., Carlut, J., Escartín, J., Mével, C., Andreani, M., & Debret, B. (2016). Magnetic signatures of serpentinization at ophiolite complexes. Geochemistry, Geophysics, Geosystems, 17, 2969–2986. https://doi.org/10.1002/2016GC006321
- Carter-Stiglitz, B., Moskowitz, B., Solheid, P., Berquó, T. S., Jackson, M., & Kosterov, A. (2006). Low-temperature magnetic behavior of multidomain titanomagnetites: TM0, TM16, and TM35. *Journal of Geophysical Research*, 111, B12S05. https://doi.org/10.1029/ 2006/JB004561
- Dai, J. G., Wang, C. S., Hébert, R., Santosh, M., Li, Y. L., & Xu, J. Y. (2011). Petrology and geochemistry of peridotites in the Zhongba ophiolite, Yarlung Zangbo Suture Zone: Implications for the Early Cretaceous intra-oceanic subduction zone within the Neo-Tethys. Chemical Geology, 288(3-4), 133-148. https://doi.org/10.1016/j.chemgeo.2011.07.011
- Day, R., Fuller, M., & Schmidt, V. A. (1977). Hysteresis properties of titanomagnetites: Grain-size and compositional dependence. Physics of the Earth and Planetary Interiors, 13(4), 260–267. https://doi.org/10.1016/0031-9201(77)90108-X
- DeCelles, P. G., Robinson, D. M., & Zandt, G. (2002). Implications of shortening in the Himalayan fold-thrust belt for uplift of the Tibetan Plateau. *Tectonics*, 21(6), 12–1. https://doi.org/10.1029/2001TC001322
- Dunlop, D. J. (2002). Theory and application of the Day plot (M_{rs}/M_s versus H_{cr}/H_c) 1. Theoretical curves and tests using titanomagnetite data. *Journal of Geophysical Research*, 107(B3), 2056. https://doi.org/10.1029/2001JB000486
- Evans, B. W., Kuehner, S. M., & Chopelas, A. (2009). Magnetite-free, yellow lizardite serpentinization of olivine websterite, Canyon Mountain complex, N.E. Oregon. American Mineralogist, 94(11-12), 1731-1734. https://doi.org/10.2138/am.2009.3301
- Ferré, E. C., Friedman, S. A., Martín-Hernández, F., Feinberg, J. M., Conder, J. A., & Ionov, D. A. (2013). The magnetism of mantle xenoliths and potential implications for sub-Moho magnetic sources. Geophysical Research Letters, 40, 105–110. https://doi.org/10.1029/ 2012GL054100
- Frost, B. R., & Beard, J. S. (2007). On silica activity and serpentinization. Journal of Petrology, 48(7), 1351–1368. https://doi.org/10.1093/petrology/egm021
- Fujii, M., Okino, K., Sato, T., Sato, H., & Nakamura, K. (2016). Origin of magnetic highs at ultramafic hosted hydrothermal systems: Insights from the Yokoniwa site of Central Indian Ridge. Earth and Planetary Science Letters, 441, 26–37. https://doi.org/10.1016/j.epsl.2016.02.018
- Groppo, C., Rinaudo, C., Cairo, S., Gastaldi, D., & Compagnoni, R. (2006). Micro-Raman spectroscopy for a quick and reliable identification of serpentine minerals from ultramafics. European Journal of Mineralogy, 18(3), 319–329. https://doi.org/10.1127/0935-1221/2006/0018-0210
- Harrison, R. J., & Feinberg, J. M. (2008). FORCinel: An improved algorithm for calculating first-order reversal curve distributions using locally weighted regression smoothing. Geochemistry, Geophysics, Geosystems, 9, Q05016. https://doi.org/10.1029/2008GC001987
- He, L. F., Hu, X. M., Zha, Y. B., Xu, L. G., & Wang, Y. H. (2014). Distribution and origin of high magnetic anomalies at Luobusa Ophiolite in Southern Tibet. Chinese Science Bulletin, 59(23), 2898–2908. https://doi.org/10.1007/s11434-014-0330-6
- Hébert, R., Bezard, R., Guilmette, C., Dostal, J., Wang, C. S., & Liu, Z. F. (2012). The Indus-Yarlung Zangbo ophiolites from Nanga Parbat to Namche Barwa syntaxes, southern Tibet: First synthesis of petrology, geochemistry, and geochronology with incidences on geodynamic reconstructions of Neo-Tethys. Gondwana Research, 22(2), 377–397. https://doi.org/10.1016/j.gr.2011.10.013
- Heslop, D., & Roberts, A. P. (2012). A method for unmixing magnetic hysteresis loops. Journal of Geophysical Research, 117, B03103. https://doi.org/10.1029/2011JB008859
- Hodel, F., Macouin, M., Triantafyllou, A., Carlut, J., Berger, J., Rousse, S., et al. (2017). Unusual massive magnetite veins and highly altered Cr-spinels as relics of a Cl-rich acidic hydrothermal event in Neoproterozoic serpentinites (Bou Azzer ophiolite, Anti-Atlas, Morocco). Precambrian Research, 300, 151–167. https://doi.org/10.1016/j.precamres.2017.08.005
- Huang, R. F., Lin, C. T., Sun, W. D., Ding, X., Zhan, W. H., & Zhu, J. H. (2017). The production of iron oxide during peridotite serpentinization: Influence of pyroxene. Geoscience Frontiers, 8(6), 1311–1321. https://doi.org/10.1016/j.gsf.2017.01.001
- Jackson, M., & Solheid, P. (2010). On the quantitative analysis and evaluation of magnetic hysteresis data. Geochemistry, Geophysics, Geosystems, 11, Q04Z15. https://doi.org/10.1029/2009GC002932
- Jiang, M., Yang, J. S., Zhang, L. S., Zhang, Y. W., Peng, M., & Li, Q. Q. (2016). The magnetic anomaly characteristics of Dongpo, Xigaze and some other ophiolite rock masses along the Yarlung–Zangbo suture zone and their ore-prospecting significance (in Chinese with English abstract). Geology in China, 43(5), 1666–1678.
- Jiang, M., Yang, J. S., Zhang, Y. W., Tan, H. D., Peng, M., Wu, L. S., et al. (2013). Deep tectonic characteristics and ore-prospecting potential of the Zetang Cr-bearing ultramafic rock mass in Tibet (in Chinese with English abstract). Geology in China, 40(3), 780–789.
- Klein, F., Bach, W., Humphris, S. E., Kahl, W., Jöns, N., Moskowitz, B., & Berquó, T. S. (2014). Magnetite in seafloor serpentinite—Some like it hot. Geology, 42(2), 135–138. https://doi.org/10.1130/G35068.1
- Klein, F., Bach, W., Jöns, N., McCollom, T., Moskowitz, B., & Berquó, T. (2009). Iron partitioning and hydrogen generation during ser-pentinization of abyssal peridotites from 15°N on the Mid-Atlantic Ridge. Geochimica et Cosmochimica Acta, 73(22), 6868–6893. https://doi.org/10.1016/j.gca.2009.08.021
- Klein, F., Bach, W., & McCollom, T. M. (2013). Compositional controls on hydrogen generation during serpentinization of ultramafic rocks. Lithos, 178, 55–69. https://doi.org/10.1016/j.lithos.2013.03.008
- Li, Z. Y., Zheng, J. P., Liu, Q. S., Griffin, W. L., & Hu, X. Y. (2015). Magnetically stratified continental lower crust preserved in the North China Craton. Tectonophysics, 643, 73–79. https://doi.org/10.1016/j.tecto.2014.12.012

LI ET AL. 14 of 15



- Li, Z. Y., Zheng, J. P., Moskowitz, B. M., Liu, Q. S., Xiong, Q., Yang, J. S., & Hu, X. Y. (2017). Magnetic properties of serpentinized peridotites from the Dongbo ophiolite, SW Tibet: Implications for suture-zone magnetic anomalies. *Journal of Geophysical Research: Solid Earth*, 122, 4814–4830. https://doi.org/10.1002/2017JB014241
- Maffione, M., Morris, A., Plümper, O., & van Hinsbergen, D. J. J. (2014). Magnetic properties of variably serpentinized peridotites and their implication for the evolution of oceanic core complexes. Geochemistry, Geophysics, Geosystems, 15, 923–944. https://doi.org/10.1002/ 2013GC004993
- Marcaillou, C., Muñoz, M., Vidal, O., Parra, T., & Harfouche, M. (2011). Mineralogical evidence for H2 degassing during serpentinization at 300°C/300bar. Earth and Planetary Science Letters, 303(3-4), 281–290. https://doi.org/10.1016/j.epsl.2011.01.006
- Mayhew, L. E., Ellison, E. T., Miller, H. M., Kelemen, P. B., & Templeton, A. S. (2018). Iron transformations during low temperature alteration of variably serpentinized rocks from the Samail ophiolite, Oman. Geochimica et Cosmochimica Acta, 222, 704–728. https://doi. org/10.1016/j.gca.2017.11.023
- McCollom, T. M., & Bach, W. (2009). Thermodynamic constraints on hydrogen generation during serpentinization of ultramafic rocks. Geochimica et Cosmochimica Acta, 73(3), 856–875. https://doi.org/10.1016/j.gca.2008.10.032
- McCollom, T. M., Klein, F., Robbins, M., Moskowitz, B., Berquó, T. S., Jöns, N., et al. (2016). Temperature trends for reaction rates, hydrogen generation, and partitioning of iron during experimental serpentinization of olivine. Geochimica et Cosmochimica Acta, 181, 175–200. https://doi.org/10.1016/j.gca.2016.03.002
- McDermid, I. R. C., Aitchison, J. C., Davis, A. M., Harrison, T. M., & Grove, M. (2002). The Zedong terrane: A Late Jurassic intra-oceanic magmatic arc within the Yarlung-Tsangpo suture zone, southeastern Tibet. Chemical Geology, 187(3-4), 267-277. https://doi.org/ 10.1016/S0009-2541(02)00040-2
- Miller, D. J., & Christensen, N. I. (1997). Seismic velocities of lower crustal and upper mantle rocks from the slow-spreading Mid-Atlantic Ridge, south of the Kane Transform Zone (MARK). In J. A. Karson, et al. (Eds.), Proceedings of the Ocean Drilling Program, scientific results (Vol. 153, pp. 437–454). Texus: College Station. https://doi.org/10.2973/odp.proc.sr.153.043.1997
- Oufs, O., Cannat, M., & Horen, H. (2002). Magnetic properties of variably serpentinized abyssal peridotites. *Journal of Geophysical Research*, 107(B5), 2095. https://doi.org/10.1029/2001JB000549
- Özdemir, Ö., & Dunlop, D. J. (2010). Hallmarks of maghemitization in low-temperature remanence cycling of partially oxidized magnetite nanoparticles. *Journal of Geophysical Research*, 115, B02101. https://doi.org/10.1029/2009JB006756
- Pike, C. R., Roberts, A. P., Dekkers, M. J., & Verosub, K. L. (2001). An investigation of multi-domain hysteresis mechanisms using FORC diagrams. Physics of the Earth and Planetary Interiors, 126(1-2), 11-25. https://doi.org/10.1016/S0031-9201(01)00241-2
- Rinaudo, C., Gastaldi, D., & Belluso, E. (2003). Characterization of chrysotile, antigorite and lizardite by FT-Raman spectroscopy. Canadian Mineralogist, 41(4), 883–890. https://doi.org/10.2113/gscanmin.41.4.883
- Roberts, A. P., Heslop, D., Zhao, X., & Pike, C. R. (2014). Understanding fine magnetic particle systems through use of first-order reversal curve diagrams. Reviews of Geophysics, 52, 557–602. https://doi.org/10.1002/2014RG000462
- Roberts, A. P., Hu, P. X., Harrison, R. J., Heslop, D., Muxworthy, A. R., Oda, H., et al. (2019). Domain state diagnosis in rock magnetism: Evaluation of potential alternatives to the day diagram. *Journal of Geophysical Research: Solid Earth*, 124, 5286–5314. https://doi.org/10.1029/2018JB017049
- Salisbury, M. H., Shinohara, M., Richter, C., & Shipboard Scientific Party (2002). Proceedings of the Ocean Drilling Program, Initial Reports (Vol. 195). College Station, TX: Ocean Drilling Program. https://doi.org/10.2973/odp.proc.ir.195.103.2002
- Stokking, L. B., Merrill, D. L., Haston, R. B., Ali, J. R., & Saboda, K. L. (1992). Rock magnetic studies of serpentinite seamounts in the Mariana and Izu-Bonin regions. In P. Fryer J. A. Pearce & L. B. Stokking, et al. (Eds.), Proceedings of the Ocean Drilling Program, Scientific Results (Vol. 125, pp. 561–580). College Station, TX: Ocean Drilling Program. https://doi.org/10.2973/odp.proc.sr.125.158.1992
- Szitkar, F., & Murton, B. J. (2018). Near-seafloor magnetic signatures unveil serpentinization dynamics at ultramafic-hosted hydrothermal sites. Geology, 46(12), 1055–1058. https://doi.org/10.1130/G45326.1
- Tauxe, L., Bertram, H. N., & Seberino, C. (2002). Physical interpretation of hysteresis loops: Micromagnetic modeling of fine particle magnetite. Geochemistry, Geophysics, Geosystems, 3(10), 1055. https://doi.org/10.1029/2001GC000241
- Toft, P. B., Arkani-Hamed, J., & Haggerty, S. E. (1990). The effects of serpentinization on density and magnetic susceptibility: A petrophysical model. Physics of the Earth and Planetary Interiors, 65(1-2), 137-157. https://doi.org/10.1016/0031-9201(90)90082-9
- Wang, J., Yao, C. L., & Li, Z. L. (2020). Aeromagnetic anomalies in central Yarlung-Zangbo suture zone (southern Tibet) and their geological origins. *Journal of Geophysical Research: Solid Earth*, 125, e2019JB017351. https://doi.org/10.1029/2019JB017351
- Wang, J. P., Li, X. W., Ning, W. B., Kusky, T., Wang, L., Polat, A., & Deng, H. (2019). Geology of a Neoarchean suture: Evidence from the Zunhua ophiolitic mélange of the Eastern Hebei Province, North China Craton. GSA Bulletin, 131(11–12), 1943–1964. https://doi.org/ 10.1130/B35138.1
- Wu, F. Y., Liu, C. Z., Zhang, L. L., Zhang, C., Wang, J. G., Ji, W. Q., & Liu, X. C. (2014). Yarlung Zangbo ophiolite: A critical updated view (in Chinese with English abstract). Acta Petrologica Sinica. 30(2), 293–325.
- Xiong, Q., Griffin, W. L., Zheng, J. P., O'Reilly, S. Y., Pearson, N. J., Xu, B., & Belousova, E. A. (2016). Southward trench migration at ~130—120 Ma caused accretion of the Neo-Tethyan forearc lithosphere in Tibetan ophiolites. Earth and Planetary Science Letters, 438, 57–65. https://doi.org/10.1016/j.epsl.2016.01.014
- Xiong, Q., Griffin, W. L., Zheng, J. P., Pearson, N. J., & O'Reilly, S. Y. (2017). Two-layered oceanic lithospheric mantle in a Tibetan ophiolite produced by episodic subduction of Tethyan slabs. Geochemistry, Geophysics, Geosystems, 18, 1189–1213. https://doi.org/10.1002/ 2016GC006681
- Yao, Z. X., Zhou, F. H., Xue, D. J., Liu, Z. J., & Zhang, Y. J. (2001). The property of the Yarlung Zangbo River aeromagnetic anomaly zone and its significance (in Chinese with English abstract). Geophysical and Geochemical Exploration, 25(4), 241–252.

LI ET AL. 15 of 15